Hybrid Domain-Decomposition/Physical-Optics Analysis of Finite Reconfigurable Reflectarrays Using Characteristic-Mode Macro Basis

Citation for the original published paper (version of record):
Lin, D., Manholm, L., Talcoth, O. et al (2026). Hybrid Domain-Decomposition/Physical-Optics Analysis of Finite Reconfigurable Reflectarrays
Using Characteristic-Mode Macro Basis Functions. IEEE Antennas and Wireless Propagation Letters, 25(7): 3018-3022. http://dx.doi.org/10.1109/LAWP.2026.3697885

(article starts on next page)

Hybrid Domain-Decomposition/Physical-Optics Analysis of Finite Reconfigurable Reflectarrays Using Characteristic-Mode Macrobasis Functions

Dijun Lin, *Graduate Student Member, IEEE*, Lars Manholm, Oskar Talcoth, Parisa Aghdam, and Rob Maaskant, *Senior Member, IEEE*

Dedicated to the memory of Songdan Wu, whose encouragement and inspiration were invaluable.

***Abstract*—This letter presents an efficient hybrid domain-decomposition/physical-optics framework for analyzing finite, large-scale reflectarrays and reconfigurable intelligent surfaces. The structure is decomposed into exterior and interior domains coupled through a generalized aperture-admittance formulation. The exterior response is approximated using physical optics, while element behavior is captured through admittance operators. Scalability to large arrays and many tuning states is achieved via a macrobasis function expansion of the aperture current, which enables multistate analysis by reusing precharacterized element operators and updating only the elements that change state. Results for 8 × 8 and 20 × 20 arrays under different illuminations closely match full-wave references while substantially reducing memory usage and simulation time, demonstrating suitability for fast analysis and optimization of reconfigurable arrays.**

***Index Terms*—Domain decomposition, generalized admittance, macrobasis functions, method of moments (MoM), physical optics (PO), reconfigurable intelligent surface (RIS), reflectarray.**

I. Introduction

RECONFIGURABLE intelligent surfaces (RIS) and reflectarrays manipulate electromagnetic wave propagation through controlled reflection responses, and they have been widely studied as potential cost-effective solutions for beam steering and coverage enhancement in beyond 5G and 6G scenarios. Reflectarrays achieve phased-array-like behavior using passive elements, whereas RIS extends this concept by allowing the element response to be tuned in operation [1], [2], [3], [4].

Accurate modeling of *finite* reflectarray and RIS apertures remains challenging. Periodic boundary conditions and infinite-array assumptions are computationally efficient, but their accuracy degrades for finite or aperiodic layouts, where edge effects and spatially varying mutual coupling become significant [5], [6], [7], [8]. In addition, cavity-backed elements have received increased attention due to their broadband potential [9], [10], [11], [12], [13]. This trend motivates scalable solvers that can explicitly represent an interior cavity region. While full-wave volumetric methods can capture these effects, they often become prohibitively expensive for large arrays and for analyses of many tuning states. Surface-integral-equation formulations, particularly the method of moments (MoM), are attractive for open-region problems because they require only surface discretization [14], [15], [16], [17], [18]. However, for large reconfigurable apertures, updating element states may still require repeated solves and matrix updates, which can limit scalability.

This letter proposes a hybrid domain-decomposition/physical-optics (DDM–PO) framework for efficient analysis of finite, large-scale reconfigurable reflectarrays and RIS. Two contributions are introduced. First, a magnetic-field integral equation (MFIE– PO) aperture-admittance formulation replaces the exterior MFIE operator with a physical-optics (PO) substitution, avoiding an explicit exterior integral-equation solve for electrically large arrays [19], [20], [21], [22], [23]. Second, the interior domain is modeled using element admittance operators together with a macrobasis function (MBF) representation, enabling multistate analysis by reusing precomputed element operators and updating only the matrix blocks associated with elements that change state [24].

The rest of this letter is organized as follows. Section II presents the formulation. Section III reports validation results and benchmarks. Finally, Section IV concludes this letter.

II. Generalized Admittance Formulation

The scattering problem for a cavity-backed reflectarray [see Fig. 1(a)] is decomposed into *exterior* and *interior* domains separated by the aperture surface S [see Fig. 1(b)]. Enforcing tangential magnetic-field continuity on S and applying field equivalence yield the MFIE on the aperture [19], [21], [25], [26]

$$\left[\boldsymbol{H}^a(\boldsymbol{M}_s)+\boldsymbol{H}^b(\boldsymbol{M}_s)\right]_{\tan}+\left[\boldsymbol{H}^a(\boldsymbol{J}_s^a)-\boldsymbol{H}^b(\boldsymbol{J}_s^b)\right]_{\tan} = \left[\boldsymbol{H}^{b,i}-\boldsymbol{H}^{a,i}\right]_{\tan}. \quad (1)$$

Here, $\boldsymbol{M}_s$ is the equivalent aperture magnetic current and is oppositely oriented on the two sides of S. The quantities $\boldsymbol{J}_s^a$ and $\boldsymbol{J}_s^b$ denote the equivalent electric currents on the exterior and interior sides, respectively. The operators $\boldsymbol{H}^a(\cdot)$ and $\boldsymbol{H}^b(\cdot)$ are the corresponding magnetic-field integral operators. The terms $\boldsymbol{H}^{a,i}$ and $\boldsymbol{H}^{b,i}$ represent any impressed magnetic fields in the

Received 11 March 2026; revised 22 May 2026; accepted 26 May 2026. Date of publication 27 May 2026; date of current version 9 July 2026. This work was supported by the European Union through ANTERRA under Grant 101072363 HORIZON-MSCA-2021-DN-01. *(Corresponding author: Dijun Lin.)*

Dijun Lin and Rob Maaskant are with the Antenna Group, Department of Electrical Engineering, Chalmers University of Technology, 412 96 Gothenburg, Sweden (e-mail: dijun@chalmers.se; rob.maaskant@chalmers.se).

Lars Manholm, Oskar Talcoth, and Parisa Aghdam are with the Ericsson Research, 412 96 Gothenburg, Sweden (e-mail: lars.manholm@ericsson.com; oskar.talcoth@ericsson.com; parisa.aghdam@ericsson.com).

Digital Object Identifier 10.1109/LAWP.2026.3697885

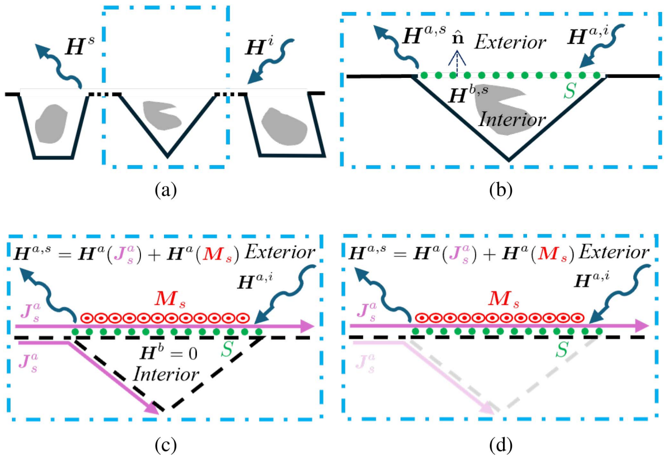

Fig. 1. Formulation steps for a cavity-backed reflectarray. (a) Scattering problem with $\boldsymbol{H}^i$ and $\boldsymbol{H}^s$. (b) Aperture S splits the exterior region a and interior cavity region b. (c) Equivalence principle on S introduces $\boldsymbol{M}_s$ and sets the fields in b to zero. (d) Neglecting rear-surface currents, the 3-D conductor is replaced by a 2-D PEC sheet in the aperture plane.

exterior and interior regions. For reference, Fig. 1(c) illustrates an exterior-only formulation obtained by setting the interior fields to zero; by the equivalence principle, this yields the same exterior fields as the original scattering configuration in Fig. 1(a).

A. PO Approximation and MFIE-PO Substitution

The structure is assumed to be backed by a perfect electric conductor (PEC), such that fields on the rear surface can be neglected. Under this assumption, the original 3-D conducting geometry is reduced to an equivalent 2-D PEC sheet coincident with the aperture plane (seen from the exterior region) [22], as illustrated in Fig. 1(d). This reduction enables an efficient treatment of the exterior domain using PO.

For a PEC boundary, the induced electric surface current density on the exterior side is

$$\boldsymbol{J}^a_s = \hat{\boldsymbol{n}} \times \boldsymbol{H}^a_{\text{tot}} \tag{2}$$

where $\hat{\boldsymbol{n}}$ is the unit normal directed into the exterior region and $\boldsymbol{H}^a_{\text{tot}} = \boldsymbol{H}^{a,i} + \boldsymbol{H}^{a,s}$ denotes the total magnetic field evaluated on the surface. In the PO approximation, the illuminated portion of a smooth, electrically large PEC surface is modeled locally as an infinite tangent plane. The shadow region is assumed to carry negligible current [23], [27], [28].

Starting from the MFIE (1) on the reduced PEC sheet, see Fig. 2(a), we treat the two PO-driven excitation cases separately and then combine them by superposition. The exterior equivalent current is written as

$$\boldsymbol{J}^a_s = \boldsymbol{J}^a_{\boldsymbol{M}_s} + \boldsymbol{J}^a_{\boldsymbol{H}^{a,i}} \tag{3}$$

where $\boldsymbol{J}^a_{\boldsymbol{M}_s}$ is the exterior current induced by the field radiated by $\boldsymbol{M}_s$ [see Fig. 2(b)] when $\boldsymbol{H}^{a,i} = \mathbf{0}$, and $\boldsymbol{J}^a_{\boldsymbol{H}^{a,i}}$ is the exterior current induced by $\boldsymbol{H}^{a,i}$ when $\boldsymbol{M}_s = \mathbf{0}$ [see Fig. 2(c)].

Case 1 (See Fig. 2(b), driven by $\boldsymbol{M}_s$): Under the PO approximation, the field $\boldsymbol{H}^a(\boldsymbol{M}_s)$ cancels $\boldsymbol{H}^a(\boldsymbol{J}^a_{\boldsymbol{M}_s})$ in the immediate shadow region. Consequently, in the illuminated region

$$\left[\boldsymbol{H}^a(\boldsymbol{J}^a_{\boldsymbol{M}_s})\right]_{\tan} \approx \left[\boldsymbol{H}^a(\boldsymbol{M}_s)\right]_{\tan}. \tag{4}$$

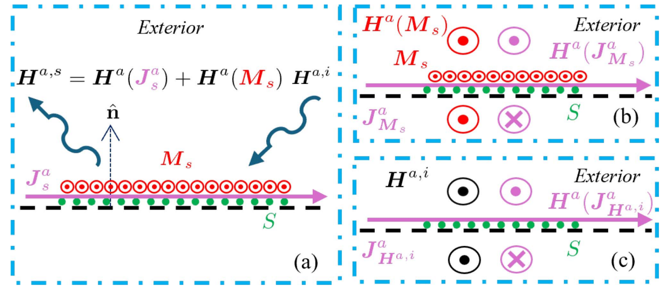

Fig. 2. Superposition used for the PO treatment of the exterior domain. (a) Reduced configuration on the aperture with equivalent magnetic current $\boldsymbol{M}_s$. (b) Contribution driven by $\boldsymbol{M}_s$, which induces the PO current $\boldsymbol{J}^a_{\boldsymbol{M}_s}$. (c) Contribution driven by the incident field $\boldsymbol{H}^{a,i}$, which induces $\boldsymbol{J}^a_{\boldsymbol{H}^{a,i}}$. The total exterior field is the sum of (b) and (c).

Case 2 (See Fig. 2(c), driven by $\boldsymbol{H}^{a,i}$): Similarly, the PO approximation in the illuminated region yields

$$\left[\boldsymbol{H}^a(\boldsymbol{J}^a_{\boldsymbol{H}^{a,i}})\right]_{\tan} \approx \left[\boldsymbol{H}^{a,i}\right]_{\tan}. \tag{5}$$

By linearity, the total exterior tangential field due to $\boldsymbol{J}^a_s$ [see Fig. 2(a)] is obtained by superposition

$$\left[\boldsymbol{H}^a(\boldsymbol{J}^a_s)\right]_{\tan} = \left[\boldsymbol{H}^a(\boldsymbol{M}_s) + \boldsymbol{H}^{a,i}\right]_{\tan} \tag{6}$$

where (3) has been substituted in the left-hand side of (6) leading to the right-hand side when using (4) and (5).

Substituting (6) into (1) yields the MFIE-PO

$$\begin{aligned}\left[2\boldsymbol{H}^a(\boldsymbol{M}_s) + \boldsymbol{H}^b(\boldsymbol{M}_s)\right]_{\tan} - \left[\boldsymbol{H}^b(\boldsymbol{J}^b_s)\right]_{\tan} \\ = \left[\boldsymbol{H}^{b,i} - 2\boldsymbol{H}^{a,i}\right]_{\tan}.\end{aligned} \tag{7}$$

A matrix representation is then obtained by discretizing (7) and applying Galerkin testing with Rao–Wilton–Glisson (RWG) basis functions, leading to tested terms of the form $\langle \mathbf{u}, \boldsymbol{H}(\mathbf{v})\rangle \triangleq \int_S \mathbf{u} \cdot \boldsymbol{H}(\mathbf{v})\, \mathrm{d}S$, where $\mathbf{u}$ and $\mathbf{v}$ denote RWG expansions of equivalent currents on the aperture surface S.

No impressed sources are assumed to exist in the interior region, $\boldsymbol{H}^{b,i} = \mathbf{0}$. Expanding $\boldsymbol{M}_s = \sum_{n=1}^{N_M} V_n \boldsymbol{f}^M_n$ in (7) and testing with $\boldsymbol{f}^M_m$ yield

$$\begin{aligned}&2\sum_{n=1}^{N_M} V_n \left\langle \boldsymbol{f}^M_m, \boldsymbol{H}^a(\boldsymbol{f}^M_n)\right\rangle + \sum_{n=1}^{N_M} V_n \left\langle \boldsymbol{f}^M_m, \boldsymbol{H}^b(\boldsymbol{f}^M_n)\right\rangle \\ &- \sum_{n=1}^{N_M} V_n \left\langle \boldsymbol{f}^M_m, \boldsymbol{H}^b(\boldsymbol{J}^b_s(-\boldsymbol{f}^M_n))\right\rangle = -2\left\langle \boldsymbol{f}^M_m, \boldsymbol{H}^{a,i}\right\rangle\end{aligned} \tag{8}$$

for $m = 1, 2, \ldots, N_M$, where the induced current $\boldsymbol{J}^b_s(-\boldsymbol{f}^M_n)$ due to $-\boldsymbol{M}_s$ on the interior is given in [19, eq. (18)].

Finally, this yields the generalized aperture-admittance system of linear equations

$$\left[\mathbf{Y}^a_{\text{tot}} + \mathbf{Y}^b_{\text{tot}}\right] \mathbf{V} = \mathbf{I} \tag{9a}$$

$$\left[\mathbf{Y}^a_{\text{tot}}\right]_{mn} = 2\left\langle \boldsymbol{f}^M_m, \boldsymbol{H}^a(\boldsymbol{f}^M_n)\right\rangle \tag{9b}$$

$$[\mathbf{I}]_m = -2\left\langle \boldsymbol{f}^M_m, \boldsymbol{H}^{a,i}\right\rangle \tag{9c}$$

$$\left[\mathbf{Y}^b_{\text{tot}}\right]_{mn} = \left\langle \boldsymbol{f}^M_m, \boldsymbol{H}^b(\boldsymbol{f}^M_n)\right\rangle - \left\langle \boldsymbol{f}^M_m, \boldsymbol{H}^b(\boldsymbol{J}^b_s(-\boldsymbol{f}^M_n))\right\rangle \tag{9d}$$

where $\mathbf{V} = [V_1, \ldots, V_{N_M}]^{\mathrm{T}}$ collects the RWG coefficients of $\boldsymbol{M}_s$, and $\mathbf{I}$ is the tested excitation.

B. Interior Domain and Macrobasis Representation

The interior domain is modeled by the cavity-admittance matrix $\mathbf{Y}^b_{\text{tot}}$, which is block diagonal with one self-admittance block per array element. Suppose that the array contains L elements drawn from P unique element types. Element l is assigned a type index $\tau(l) \in \{1, \ldots, P\}$, so

$$\mathbf{Y}^b_{\text{tot}} = \text{blkdiag}\left(\mathbf{Y}^{b,(\tau(1))}, \ldots, \mathbf{Y}^{b,(\tau(L))}\right) \tag{10}$$

i.e., each unique type is analyzed once and reused across the array [24]. For MBF generation, each element is treated as a nonoverlapping unit-cell analysis region; no buffer or overlap region is introduced. After assembly, interelement interactions are included through the global aperture-admittance system, with array-level coupling provided by the MFIE–PO exterior formulation.

To reduce the number of unknowns without changing the MFIE–PO formulation, the aperture magnetic current is expanded through MBFs [29], [30]. Let $\mathbf{V} \in \mathbb{C}^N$ collect the RWG coefficients of $\boldsymbol{M}_s$ on the aperture.

The MBF reduction is written as $\mathbf{V} = \mathbf{V}_{\text{MBF}}\mathbf{w}$, where $\mathbf{V}_{\text{MBF}} \in \mathbb{C}^{N\times K}$ contains the MBFs in the original basis. The vector $\mathbf{w}$ stacks the MBF weights for all elements, with K_l MBFs retained for element l. Accordingly, $K = \sum_{l=1}^{L} K_l$, and $\mathbf{V}_{\text{MBF}}$ is assembled elementwise as a block-diagonal matrix with blocks $\mathbf{V}^{(\tau(1))}_{\text{MBF}}, \ldots, \mathbf{V}^{(\tau(L))}_{\text{MBF}}$.

Substituting this expansion into (9a) yields the reduced system

$$\left(\mathbf{V}^{\text{T}}_{\text{MBF}} \left[\mathbf{Y}^a_{\text{tot}} + \mathbf{Y}^b_{\text{tot}}\right] \mathbf{V}_{\text{MBF}}\right) \mathbf{w} = \mathbf{V}^{\text{T}}_{\text{MBF}}\mathbf{I}. \tag{11}$$

Once $\mathbf{w}$ is solved, the full-resolution current follows from $\mathbf{V} = \mathbf{V}_{\text{MBF}}\mathbf{w}$.

1) MBF Generation via Characteristic Mode Analysis: MBFs are computed once for each unique element type. For P element types, we form the local composite admittance $\mathbf{Y}^{(\tau(p))} = \mathbf{Y}^{a,(\tau(p))}_{\text{tot}} + \mathbf{Y}^{b,(\tau(p))}_{\text{tot}}$ and write $\mathbf{Y}^{(\tau(p))} = \mathbf{G}^{(\tau(p))} + j\mathbf{B}^{(\tau(p))}$, where $\mathbf{G}^{(\tau(p))} = \frac{1}{2}(\mathbf{Y}^{(\tau(p))} + \mathbf{Y}^{(\tau(p))\text{H}})$ and $\mathbf{B}^{(\tau(p))} = \frac{1}{2j}(\mathbf{Y}^{(\tau(p))} - \mathbf{Y}^{(\tau(p))\text{H}})$. The characteristic currents then satisfy

$$\mathbf{B}^{(\tau(p))}\mathbf{J}^{(\tau(p))}_n = \lambda^{(\tau(p))}_n \mathbf{G}^{(\tau(p))}\mathbf{J}^{(\tau(p))}_n \tag{12}$$

and are ranked using the modal significance $\text{MS}^{(\tau(p))}_n = (1 + (\lambda^{(\tau(p))}_n)^2)^{-1/2}$ [31], [32], [33]. The K_p most significant modes form the local MBF matrix $\mathbf{V}^{(\tau(p))}_{\text{MBF}}$.

2) MBF Generation via Singular Value Decomposition: Alternatively, for each unique type p, we compute the SVD of the local inverse composite admittance

$$(\mathbf{Y}^{(p)})^{-1} = \mathbf{U}^{(p)}\boldsymbol{\Sigma}^{(p)}\mathbf{D}^{(p)\text{H}} \tag{13}$$

and form the reduced basis by retaining the K_p dominant left singular vectors

$$\mathbf{V}^{(p),\text{SVD}}_{\text{MBF}} = \mathbf{U}^{(p)}(:, 1:K_p). \tag{14}$$

The number K_p is chosen near the knee of the singular-value decay curve, rather than from a universal fixed threshold, since the current-reconstruction error is generally not known a priori; more singular vectors may be retained for higher current accuracy.

Both characteristic mode analysis (CMA)-based and singular value decomposition (SVD)-based MBFs are computed once per unique element type and reused across the array. CMA yields physically interpretable, excitation-independent modes, whereas SVD provides an excitation-independent numerical orthonormal basis based on singular values. Both approaches are validated on a single element in Section III.

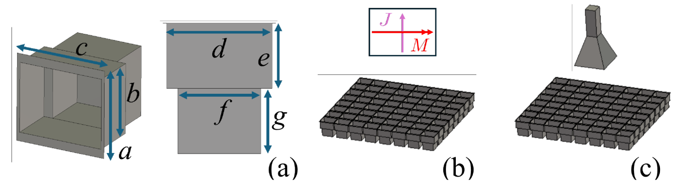

Fig. 3. (a) Reference element from [9] used to evaluate the proposed methodology, with $a = 6$ mm, $b = 5.6$ mm, $c = 5$ mm, $d = 4$ mm, $e = 3$ mm, $f = 4.4$ mm, and $g = 3$ mm. (b) 8×8 array configuration with $e = g = 3$ mm under Huygens-source illumination at 10 cm. (c) Same 8×8 array under horn-antenna illumination at 10 cm.

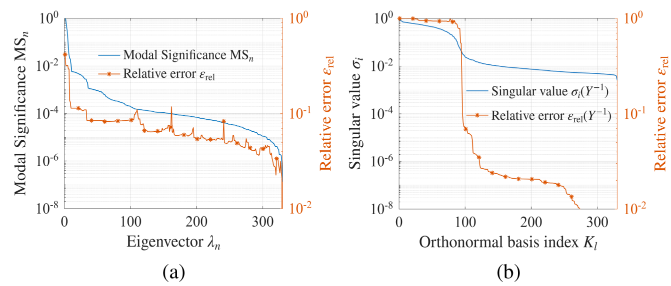

Fig. 4. (a) CMA modal significance MS_n and the corresponding reconstruction error ε_{rel} versus the number of retained characteristic modes. (b) Singular values σ_i obtained from $\mathbf{Y}^{-1}$.

C. Exterior Scattering

After solving for the aperture magnetic current $\boldsymbol{M}_s$ (via $\mathbf{V}$ or $\mathbf{w}$), the exterior scattering is evaluated from the PO current $\mathbf{J}_{\text{PO}} = 2\hat{\mathbf{n}} \times (\mathbf{H}^{a,i} + \mathbf{H}^a(\mathbf{M}_s))$. With MBF reduction, solving for $\boldsymbol{M}_s$ scales as $\mathcal{O}(K^3)$, and the subsequent PO current evaluation scales as $\mathcal{O}(N)$.

III. Results

Validation is carried out at 32 GHz for an unmodulated 8×8 reflectarray and a modulated 20×20 reflectarray. The element geometry is shown in Fig. 3(a) and is based on [9] with minor parameter adjustments. A Huygens source is used to realize minimal edge taper, while a high-gain horn provides a strongly tapered excitation. In all cases, the feed is modeled as a far-field source and feed–array coupling is neglected.

The impact of MBF reduction is first assessed on a single element illuminated by the Huygens source at a distance of 10 cm ($\approx 10.7\lambda$). Fig. 4(a) reports the CMA modal significance, while Fig. 4(b) shows the singular spectrum obtained from $\mathbf{Y}^{-1}$ and the corresponding reconstruction error. For both constructions, the reconstruction error is quantified by the relative error

$$\varepsilon_{\text{rel}} = \frac{\|\mathbf{V}_{\text{MBF}}\mathbf{w} - \mathbf{V}\|_2}{\|\mathbf{V}\|_2} \tag{15}$$

where $\mathbf{V}$ denotes the solved RWG coefficient vector of $\mathbf{M}_s$. Based on these results, subsequent array evaluations use CMA-based MBFs, which provide lower current-reconstruction error for small K_l in the considered example while remaining physically interpretable.

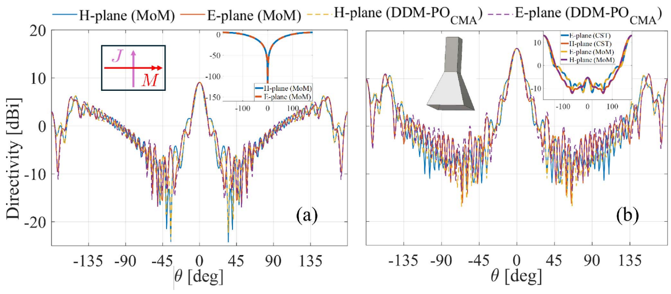

Fig. 5. Radiation patterns of the 8×8 array under (a) Huygens-source and (b) horn illumination at 10 cm ($\approx 10.7\lambda$). DDM–PO with $K_l = 10$ CMA-MBFs per element is compared with the MoM reference. Insets show the corresponding feed patterns.

TABLE I
BENCHMARKS (CMA, $K_l = 10$ MBFS PER ELEMENT) ON I9-12900 K/128 GB/RTX 3080

Array	Case	Mem	Time (s)		Unknowns	$\bar{e}$ (%)
			CPU	GPU	MBF+PO	
8×8	DDM–PO / Huy.	7 MB	< 1	64	640+35k	1.3
8×8	DDM–PO / Horn	7 MB	< 1	63	640+35k	0.6
8×8	MoM	35 GB	594	–	48k	–
20×20	DDM–PO / Horn	269 MB	171	1017	4k+219k	0.06
20×20	CST (MLFMM)	100 GB	5316	12206	1.23M	–

Times are CPU/GPU seconds; total runtime is their sum. In the MBF+PO column, $A + B$ means (A) reduced-system MBF unknowns plus (B) PO degrees of freedom used for the exterior PO-current evaluation. Here, $k = 10^3$ and $M = 10^6$.

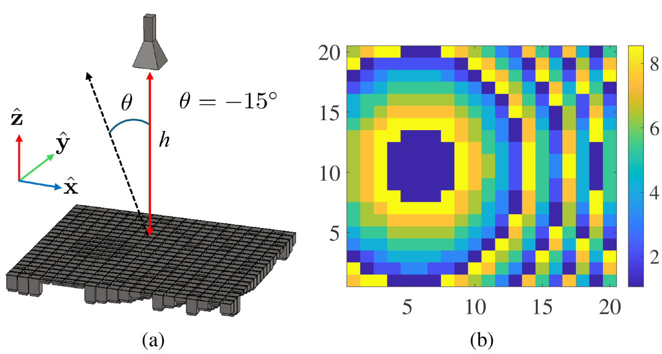

Fig. 6. (a) 20×20 reflectarray scanning to $\theta = -15°$, illuminated by a horn at $h = 10$ cm. (b) Elementwise modulation of g (in mm) using eight discrete states, with e fixed to 1 mm.

The 8×8 array is evaluated under both illumination conditions using $K_p = 10$ CMA-MBFs for the element type. As shown in Fig. 5(a) and (b), the proposed approach closely matches the MoM reference in both the E- and H-planes. The computational benefits are summarized in Table I, showing orders-of-magnitude lower memory and runtime relative to MoM (CPU+GPU time). The average relative error $\bar{e}$ is computed from the sampled radiation-pattern values x_i (linear scale) over the E- and H-planes as

$$\bar{e} = \frac{1}{N}\sum_{i=1}^{N} e_i, \qquad e_i = \frac{\left|x_i - x_i^{\mathrm{ref}}\right|}{\max_j \left|x_j^{\mathrm{ref}}\right|} \tag{16}$$

and remains within 0.6% to 1.3% for both Huygens and horn illumination.

Finally, the method is validated on a 20×20 modulated array configured to scan to $\theta = -15°$. Eight discrete element states are used, and each state is represented using $K_p = 10$ MBFs. The array geometry and modulation are shown in Fig. 6. The resulting radiation pattern is compared with CST (MLFMM, solver tol. 10^{-4}, level $= 6$) [34] in Fig. 7, since a full MoM reference would require prohibitive memory resources (about 1 TB) that are not available. The results show good agreement, while Table I indicates an over two-order-of-magnitude reduction in memory usage and a $> 10\times$ reduction in total runtime (CPU+GPU) relative to CST. Fig. 8 shows the computed $\boldsymbol{M}_s$ and induced $\boldsymbol{J}_{\mathrm{PO}}$, illustrating how the modulation shapes the current distribution across the array.

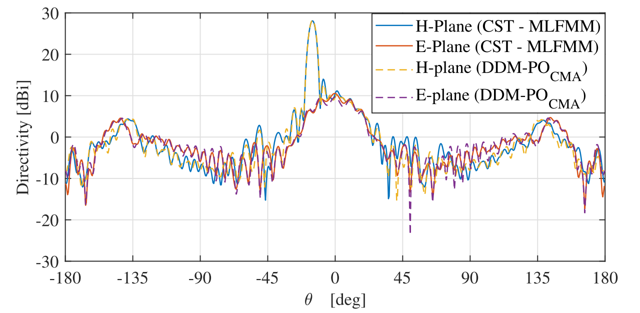

Fig. 7. Radiation patterns of the 20×20 array scanning to $\theta = -15°$, computed by DDM–PO with $K_p = 10$ CMA-MBFs per state and compared with CST MLFMM.

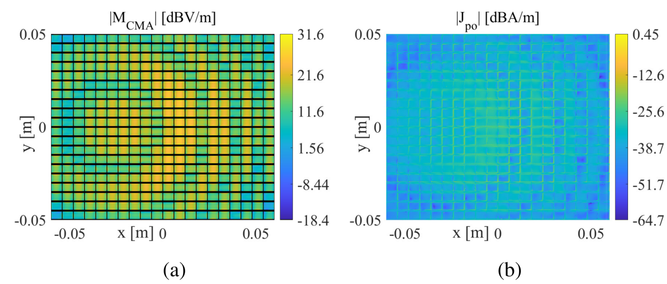

Fig. 8. (a) Magnetic current $\boldsymbol{M}_s$ using 80 CMA-MBFs (10 per state). (b) Induced PO current on the PEC.

IV. CONCLUSION

This letter presented a DDM–PO framework for analyzing large-scale reconfigurable reflectarrays and RIS. The formulation couples the interior and exterior domains through a generalized aperture-admittance system and employs PO to approximate the exterior response, enabling efficient evaluation of electrically large arrays. CMA-MBFs further reduce unknowns by reusing precharacterized element operators and updating only those elements that change state. Results for 8×8 and 20×20 arrays under different illuminations show close agreement with full-wave references while substantially reducing memory usage and simulation time. Future work will add PO edge-diffraction corrections for finite arrays.

ACKNOWLEDGMENT

Views and opinions expressed are however those of the author(s) only and do not necessarily reflect those of the European Union. Neither the European Union nor the granting authority can be held responsible for them.

REFERENCES

[1] M. Di Renzo et al., “Smart radio environments empowered by reconfigurable intelligent surfaces: How it works, state of research, and the road ahead,” *IEEE J. Sel. Areas Commun.*, vol. 38, no. 11, pp. 2450–2525, Nov. 2020.

[2] Z. Zhu, C. Pan, Q. Wu, M. Di Renzo, A. L. Swindlehurst, and Y. Zhao, “Special issue on reconfigurable intelligent surface for B5G & 6G,” *J. Commun. Netw.*, vol. 24, no. 5, pp. 513–517, 2022.

[3] S. H. Zainud-Deen, “Reconfigurable intelligent surfaces for wireless communications,” in *Proc. 39th Nat. Radio Sci. Conf.*, 2022, pp. 342–342.

[4] Y. Zhao, “Reconfigurable intelligent surfaces for 6G: Applications, challenges, and solutions,” *Front. Inf. Technol. Electron. Eng.*, vol. 24, pp. 1669–1688, 2023.

[5] H. Holter and H. Steyskal, “On the size requirement for finite phased-array models,” *IEEE Trans. Antennas Propag.*, vol. 50, no. 6, pp. 836–840, Jun. 2002.

[6] M. Zhou et al., “Investigations on accurate analysis of microstrip reflectarrays,” in *Proc. 33rd ESA Antenna Workshop Challenges Space Antenna Syst.*, Noordwijk, The Netherlands, Oct. 2011, pp. 1–7

[7] M. Inam et al., “Linearly polarized millimeter wave reflectarray with mutual coupling optimization,” *Comput., Mater. Continua*, vol. 72, no. 2, pp. 2397–2410, 2022.

[8] E. Baladi and S. V. Hum, “Equivalent circuit models for metasurfaces using floquet modal expansion of surface current distributions,” *IEEE Trans. Antennas Propag.*, vol. 69, no. 9, pp. 5691–5703, Sep. 2021.

[9] J. Zhu, Y. Yang, S. Liao, and Q. Xue, “Additively manufactured metal-only waveguide-based millimeter-wave broadband achromatic reflectarrays,” *IEEE Trans. Antennas Propag.*, vol. 71, no. 7, pp. 6185–6190, Jul. 2023.

[10] O. S. Hassan, K. H. Ali, and M. A. Abou-Khousa, “A 3-D-printed mm-wave reflectarray with coaxial unit cells,” *IEEE Trans. Antennas Propag.*, vol. 72, no. 12, pp. 9251–9258, Dec. 2024.

[11] T. Makdissy, R. Gillard, Z. An, and S. Vaudreuil, “Dual linearly polarised 3D printed phoenix cell for wide band metal only reflectarrays,” *Microw., Antennas Propag.*, vol. 14, no. 12, pp. 1411–1416, 2020.

[12] Y. H. Cho, W. J. Byun, and M. S. Song, “High gain metal-only reflectarray antenna composed of multiple rectangular grooves,” *IEEE Trans. Antennas Propag.*, vol. 59, no. 12, pp. 4559–4568, Dec. 2011.

[13] A. Gómez-Álvarez, N. Delmonte, L. Silvestri, M. Bozzi, M. Arrebola, and M. R. Pino, “Reflectarray antenna using novel SIW-based cavity resonators with a broadband performance,” *IEEE Trans. Antennas Propag.*, vol. 73, no. 10, pp. 7692–7705, Oct. 2025.

[14] W. C. Gibson, *The Method of Moments in Electromagnetics*. Boca Raton, Fl, USA:Chapman & Hall/CRC Taylor & Francis Group, 2008

[15] R. Gholami, P. Naseri, P. Triverio, and S. V. Hum, “An efficient integral equation method for full-wave analysis of inhomogeneous electromagnetic surfaces with connected conductors,” *IEEE Trans. Antennas Propag.*, vol. 70, no. 7, pp. 5647–5658, Jul. 2022.

[16] U. R. Patel, P. Triverio, and S. V. Hum, “A fast macromodeling approach to efficiently simulate inhomogeneous electromagnetic surfaces,” *IEEE Trans. Antennas Propag.*, vol. 68, no. 11, pp. 7480–7493, Nov. 2020.

[17] U. R. Patel, P. Triverio, and S. V. Hum, “A macromodeling approach to efficiently compute scattering from large arrays of complex scatterers,” *IEEE Trans. Antennas Propag.*, vol. 66, no. 11, pp. 6158–6169, Nov. 2018.

[18] I. Kim, H.-R. Im, I.-P. Hong, H. Lee, and J.-G. Yook, “An accelerated method of a generalized transition matrix model using characteristic basis functions for large-scale open-ended cavities,” *IEEE Trans. Antennas Propag.*, vol. 72, no. 8, pp. 6813–6818, Aug. 2024.

[19] R. Maaskant et al., “Domain decomposition analysis of open-cavity-based array elements - roadmap toward analyzing large-scale reflectarrays and reconfigurable intelligent surfaces,” in *Proc. Int. Conf. Electromagn. Adv. Appl.*, 2025, pp. 687–692.

[20] D. Lin, P. Aghdam, and R. Maaskant, “Modeling of conformal reflectarrays through domain decomposition using a generalized admittance approach,” in *Proc. Asia-Pacific Microw. Conf.*, 2025, pp. 1–3.

[21] R. Harrington and J. Mautz, “A generalized network formulation for aperture problems,” *IEEE Trans. Antennas Propag.*, vol. 24, no. 6, pp. 870–873, Nov. 1976.

[22] D. Lin, L. Manholm, O. Talcoth, S. Agneessens, P. Aghdam, and R. Maaskant, “Fast scattering analysis of large open-cavity based reflectarrays using a hybrid method of moment and physical optics approach,” in *Proc. 2025 Int. Conf. Electromagn. Adv. Appl.*, 2025, pp. 682–686.

[23] J. S. Asvestas, “The physical optics method in electromagnetic scattering,” *J. Math. Phys.*, vol. 21, no. 2, pp. 290–299, 1980.

[24] D. Lin, L. Manholm, and R. Maaskant, “Fast MoM-based solvers for cavity-backed reflectarrays and RIS design,” in *Proc. Eur. Conf. Antennas Propag.*, 2026, pp. 1–5.

[25] A. Booysen, “Aperture theory and the equivalence theorem,” in *Proc. IEEE Antennas Propag. Soc. Int. Symp. 1999 Digest. Held Conjunction With USNC/URSI Nat. Radio Sci. Meeting (Cat. No.99CH37010)*, 1999, pp. 1258–1261.

[26] S. A. Schelkunoff, “Some equivalence theorems of electromagnetics and their application to radiation problems,” *Bell Syst. Tech. J.*, vol. 15, no. 1, pp. 92–112, 1936.

[27] P.-S. Kildal, “On the accuracy of physical optics,” *IEEE Trans. Antennas Propag.*, vol. AP-30, no. 3, pp. 509–512, May 1982.

[28] S. Kildal, *Foundations of Antenna Engineering: A Unified Approach for Line-of-Sight and Multipath*. Gothenburg, Sweden: Kildal Antenn AB, 2021.

[29] E. Erçil, L. Alatan, and O. A. Civi, “An efficient numerical solution method for reflectarrays of varying element sizes,” *IEEE Trans. Antennas Propag.*, vol. 63, no. 12, pp. 5668–5676, Dec. 2015.

[30] S. N. Jha, C. Craeye, and S. V. Hum, “Fast MBF approach for reflectarrays analysis,” in *Proc. 8th Eur. Conf. Antennas Propag.*, 2014, pp. 2595–2597.

[31] R. Harrington and J. Mautz, “Theory of characteristic modes for conducting bodies,” *IEEE Trans. Antennas Propag.*, vol. 19, no. 5, pp. 622–628, Sep. 1971.

[32] R. Harrington and J. Mautz, “Characteristic modes for aperture problems,” *IEEE Trans. Microw. Theory Techn.*, vol. MTT-33, no. 6, pp. 500–505, Jun. 1985.

[33] X. Deng, D. Zhang, Y. Chen, and S. Yang, “Characteristic mode analysis: Application to electromagnetic radiation, scattering, and coupling problems,” *Chin. J. Electron.*, vol. 32, no. 4, pp. 663–677, 2023.

[34] Dassault Systèmes, “CST Studio Suite,” Software version 2025.05, May 30, 2025.